

RESEARCH LETTER

10.1002/2014GL062235

Key Points:

• We proposed a new χ scaling

Correspondence to:

D. J. Bogucki,
Darek.Bogucki@tamucc.edu

Citation:

Bogucki, D. J., K. Huguenard, B. K. Haus, T. M. Özgökmen, A. Reniers, and N. J. M. Laxague (2015), Scaling laws for the upper ocean temperature dissipation rate, *Geophys. Res. Lett.*, *42*, 839–846, doi:10.1002/2014GL062235.

Received 15 OCT 2014

Accepted 19 JAN 2015

Accepted article online 24 JAN 2015

Published online 10 FEB 2015

Scaling laws for the upper ocean temperature dissipation rate

Darek J. Bogucki¹, K. Huguenard¹, B. K. Haus², T. M. Özgökmen², A. Reniers³, and N. J. M. Laxague²

¹Department of Physical and Environmental Sciences, Texas A and M University-Corpus Christi, Corpus Christi, Texas, USA, ²Department of Ocean Sciences, Rosenstiel School of Marine and Atmospheric Science, University of Miami, Coral Gables, Florida, USA, ³Department of Hydraulic Engineering, Delft University of Technology, Delft, Netherlands

Abstract Our understanding of temperature dissipation rate χ within the upper ocean boundary layer, which is critical for climate forecasts, is very limited. Near-surface turbulence also affects dispersion of contaminants and biogeochemical tracers. Using high-resolution optical turbulence measurements, scaling laws for χ are investigated under forcing states where either the daytime heat flux or the wind stress forcing is dominant. We find that χ remains constant over 1.5 times the significant wave height, while over a layer below, χ decays based on the local surface forcing. When the heat flux is dominant, traditional scaling based on the Monin-Obukhov similarity theory remains valid; $\chi \propto z^{-1}$. When the wind stress dominates, we observe the emergence of a new scaling, $\chi \propto z^{-1/2}$, which is explained by invoking the effect of small-scale coherent structures on vertical heat transport. These results have implications for improved modeling of the ocean's heat and CO₂ intake.

1. Introduction

The physical processes in the upper ocean are of interest because of their importance in the transport of passive and active tracers, such as heat [Chelton et al., 2007], biogeochemical tracers [Klein and Lapeyre, 2009; Lévy et al., 2011], and buoyant pollutants [Jernelöv and Lindén, 1981; Crone and Tolstoy, 2010; Poje et al., 2014]. The upper ocean can be dynamically separated into two broad regions. The oceanic mixed layer (ML) is the upper layer of the ocean, where salinity and temperature have been vertically homogenized by active turbulence up to a depth of D . The upper ocean boundary layer (OBL) is the region subject to stresses acting on either side of the air-sea interface, resulting in enhanced waterside turbulence and vertical subsurface transport. The vertical distribution of near-surface turbulent kinetic energy dissipation rate $\epsilon = \nu \langle \partial u'_i / \partial x_j \rangle^2$ (ν is the kinematic viscosity, u'_i represents the fluctuating x , y , or z velocity component, and $\langle \rangle$ is the ensemble average) has been extensively measured and modeled [Soloviev and Lukas, 2006].

In contrast, the scaling laws of variance dissipation rates for scalars, such as temperature, within the OBL are much less documented. The temperature dissipation (TD) rate is defined as $\chi = 2k_T \langle \nabla T' \rangle^2$, where k_T is the thermal diffusivity and T' is the temperature fluctuation.

The oceanic TD rates are among the most important parameters relevant to climate dynamics. The OBL thermal inertia is estimated to add a delay in surface temperature responses to climate warming of 10 to 100 years [Trenberth, 2002]. The upper ocean turbulent heat flux, proportional to the local TD rate [Osborn and Cox, 1972], is related to the OBL thermal inertia. Furthermore, the flux of CO₂ between ocean and atmosphere depends on the air-sea exchange coefficient, which is proportional to the gas transfer velocity [Bogucki et al., 2010]. It can be directly parameterized in terms of turbulent heat diffusivity (for wind speeds in excess of 4 m/s) [Asher et al., 2004], which in turn depends on vertical χ variability.

The usefulness of the scalar scaling laws can be demonstrated as follows: the observations of Lombardo and Gregg [1989] endorse classic similarity scaling. That is, near the ocean surface the variation of the TD with depth z follows $\chi(z) = u_{*W} T_*^2 z^{-1}$, where $T_* = J_b^0 / (c_p \rho u_{*W})$, c_p is the specific heat, ρ is the water density, J_b^0 is the surface buoyancy flux, and u_{*W} is the waterside friction velocity. In turn, the friction velocity is related to shear stresses at the boundary $u_{*W}^2 = \langle u'w' \rangle_0$ or formally $\langle u'w' \rangle_0 = \int_0^\infty E_{uw}(k_x) dk_x |_{z=0}$ with $E_{uw} = \alpha \frac{dU}{dz} \epsilon^{1/3} k_x^{-7/3}$, where u' and w' are respectively horizontal and vertical fluctuating flow components, $E_{uw}(k_x)$ is their spectral representation, k_x is a wave number, and $\alpha \simeq 0.15$ [Hunt and Morrison, 2000]. Assuming that $E_{uw}(k_x)$ attains a maximum at some length scale λ_0 [Chung and Matheou, 2012], then $u_{*W}^2 = \int_{2\pi/\lambda_0}^\infty E_{uw}(k_x) dk_x |_{z=0}$ resulting in $u_{*W}^2 \propto (\lambda_0^{4/3} \frac{dU}{dz} \epsilon^{1/3}) |_{z=0}$. Thus, near-surface χ carries information

about the mean velocity shear $\frac{du}{dz}|_{z=0}$, surface buoyancy flux J_b^0 , and surface dissipation rate $\epsilon|_{z=0}$. The local values of $\epsilon|_{z=0}$ control the local mixing of momentum down through the water column, the dispersion of near-surface contaminants [Craig and Banner, 1994], the fate of dispersant-treated oil droplets [Li and Garrett, 1998], as well as phytoplankton dispersion [Cross et al., 2014].

There are a number of important reasons to study the subsurface distribution of χ . Large eddy simulation models of the upper ocean would benefit from guidance when choosing parameterizations of subgrid surface scalar fluxes [Large et al., 1994; Sander et al., 2000]. Oceanic vertical χ rates are likely the only water column turbulent quantity amenable to optical remote sensing [Bogucki et al., 2007a; Bogucki and Spiers, 2013; Dalgleish et al., 2013]. Improved understanding of χ scaling laws would enable remote global evaluations of turbulent forcing driving the oceanic ML.

The available TD models are scarce and based on very few measurements like those presented in Lombardo and Gregg [1989] and Anis [2006], with a general absence of documented observations within the upper part of the oceanic ML. The paucity of documented near-surface oceanographic observations of χ motivated us to raise the following questions: How do near-surface χ values scale with depth? Is there a layer bordering the air-sea interface where χ is depth independent; and if so, what is its thickness? Is the Monin-Obukhov Similarity Theory (MOST) deduced shear scaling [Lombardo and Gregg, 1989] a proper description of near-surface χ , when the heat flux stabilizes the ML (a condition typically experienced by the OBL during daytime observations)?

This paper aims to close the aforementioned scientific gaps by presenting the analysis of χ data from the OBL stirred by either wind stress or dominated by buoyancy forcing when the wind stress weakens. We start with an overview of existing models of χ near the surface, followed by a description of our observational program. We then compare our data to our proposed model, which explicitly attempts to incorporate the effects of coherent structures which were detected to populate the OBL in our observations.

2. Near-Surface Turbulent Dynamics

At the immediate proximity of the free surface, the normal velocity of a particle follows the normal velocity component of the surface itself. This is in contrast to a rigid wall, where the velocity at any point on the wall is zero. Despite the differences, aquatic near-surface turbulence is typically characterized by its wall layer analogue. Observations of wall layer turbulence have demonstrated that up to a distance from the wall of 20% of the outer boundary layer thickness, the flow is dominated by the wall turbulent processes [Nowell, 1983; Hunt and Morrison, 2000]. Over the depth range z of the so-called inner layer, ϵ follows the relationship [Hinze, 1959]

$$\epsilon(z) = \frac{u_{*w}^3}{\kappa z}, \quad (1)$$

where κ is the von Karman constant. The vertical structure of a realistic, pliable, and shear-driven air-sea interface is more complicated than the solid-wall counterpart. Following Terray et al. [1996], the air-sea interface is divided into three sublayers: (1) wave-affected sublayer adjacent to the air-sea interface with approximately constant ϵ there, (2) underlying sublayer where the ϵ values are larger than those predicted by equation (1), and (3) the deepest sublayer where ϵ follows the wall-like behavior given in equation (1).

The surface-affected sublayer (1) extends from the surface to a depth of $\approx 0.6H_s$ [Terray et al., 1996], where H_s is the significant wave height. Rapp and Melville [1990] observed enhanced turbulence levels reaching depths $(1.7 \pm 0.3)H$ for spilling breakers and $(2.5 \pm 0.5)H$ for plunging breakers after 13 wave periods, with H being the wave height. Below the constant ϵ layer, a second sublayer (2) develops. The third sublayer (3) appears at depth $z_t = (3.6c'/u_*)H_s$, where c' is the phase speed of waves at the peak of the wave frequency spectrum and u_* is the air-side friction velocity. When the wave age c'/u_* exceeds 13.3, the value of c' is given as $c'/c \approx 10u_*/c - 0.25$ and $c'/c \approx 0.5$ when $4 < c'/u_* < 13.3$ [Thorpe et al., 2003].

When subject to surface buoyancy flux J_b^0 , another vertical length scale emerges, namely, the Monin-Obukhov length $L \equiv -u_{*w}^3/(\kappa J_b^0)$. This scale corresponds to the depth where the wind stress and buoyancy are equally effective at producing turbulence. During daytime in the ML, the heat flux is typically directed downward, resulting in $J_b^0 < 0$ and $L > 0$. The daytime heat flux typically has a stabilizing effect on

the ML, when the mixed layer becomes progressively shallower with time [Shay and Gregg, 1986]. The situation changes at night when the ocean releases heat into the atmosphere, destabilizing the ML by setting up convective flow and deepening the ML.

3. Near-Surface Temperature Dissipation Rate

The χ scaling within the OBL is based on a first-order description of turbulence within the atmospheric planetary boundary layer (PBL) via the Monin-Obukhov Similarity Theory (MOST). According to MOST, the relevant parameters within the vicinity of the boundary are the distance from boundary z , the surface heat flux J_b^0 , and the friction velocity u_{*w} . Under MOST assumptions, χ is expected to follow [Lombardo and Gregg, 1989]

$$\chi(z) = u_{*w} T_*^2 z^{-1}. \quad (2)$$

Similarity scaling works well when the surface forcing is horizontally uniform [Large et al., 1994]. Observations in the atmospheric PBL confirmed the validity of equation (2) for $z < 0.1L$, together with an asymptotic deviation for $z \gg 0.1L$ [Hartogensis and Debruin, 2005].

To the best of our knowledge, there has not been any near-surface χ observation with daytime heat flux into the OBL. Lombardo and Gregg [1989] presented evidence that under convectively dominated ML (nighttime) when $D < -L$, the TD data conformed to the stress scaling of equation (2) within the depth interval of $0.2D \leq z \leq 0.7D$ (their Figure 16). The χ scaling for the near-surface sublayer at $0 \leq z \leq 0.2D$ was not addressed.

The observations of Sander et al. [2000] offer some indirect evidence suggesting that the stress scaling under nighttime conditions, in the form of equation (2), may not be applicable within the sublayer adjacent to the surface. More clues about the physics of near-surface scalar turbulent dynamics can be gleaned from available direct numerical simulation (DNS) studies. Komori et al. [2010] presented results from DNS of two-phase flow (gas-liquid) subject to a wind speed of around 5 m/s. Komori et al. [2010], as well as Khakpour et al. [2012], observed that the scalar transfer through the gas-liquid interface was strongly controlled by the aquatic side via downward bursting motions of coherent structures. Also, Adrian [2007] noted the presence of surface-formed coherent structure across the whole turbulent boundary layer. The boundary typically organizes flow into large-scale vortical coherent structures (horseshoe eddies and hairpin vortices) characterized by V shape (with “legs” pointing toward the surface), which in turn interact back in subtle ways with the boundary layers leading to a complex and not well-understood dynamics [Adrian, 2007]. While traveling away from boundary, these structures dissipate at the smallest flow scales—Kolmogorov length scale [Lozano-Durán and Jiménez, 2014].

Our observations reveal coherent structures within the OBL (Figures 1a and 1b), as predicted by DNS. The presence of coherent structures may contribute to deviations from MOST assumptions. Next, we posit a model for temperature variance decay associated with coherent structures and then evaluate its validity using an analysis of our observations.

4. Effect of Coherent Structures on Vertical Scalar Transport

The presence of coherent structures mediating the vertical scalar transport indicates that MOST assumptions need to be suitably modified in order to properly describe near-surface scalar dissipation. The presence and action of coherent scalar structures with their downward bursting motion introduce intrinsic length and time scales that are not considered within the scope of MOST.

Accordingly, we augment the MOST theory with an additional parameter, namely, the Kolmogorov time scale $t_k = (\nu/\epsilon)^{1/2}$, which describes the characteristic evolution time of the smallest eddies present in the flow [Tennekes and Lumley, 1972]. The introduction of t_k (and therefore ν) into MOST assumptions is needed, because typically, the largest temperature gradients and sources of turbulent temperature fluctuations T'_0 are contained within a few centimeters below the air-sea boundary [Soloviev and Schlüssel, 1996]. Upon entering the constant stress layer, the water parcel is carried down by coherent structures. The water parcel's temperature variance T'^2_0 will begin to decay over t_k , yielding $\chi = T'^2_0/t_k$ locally. Therefore, it is

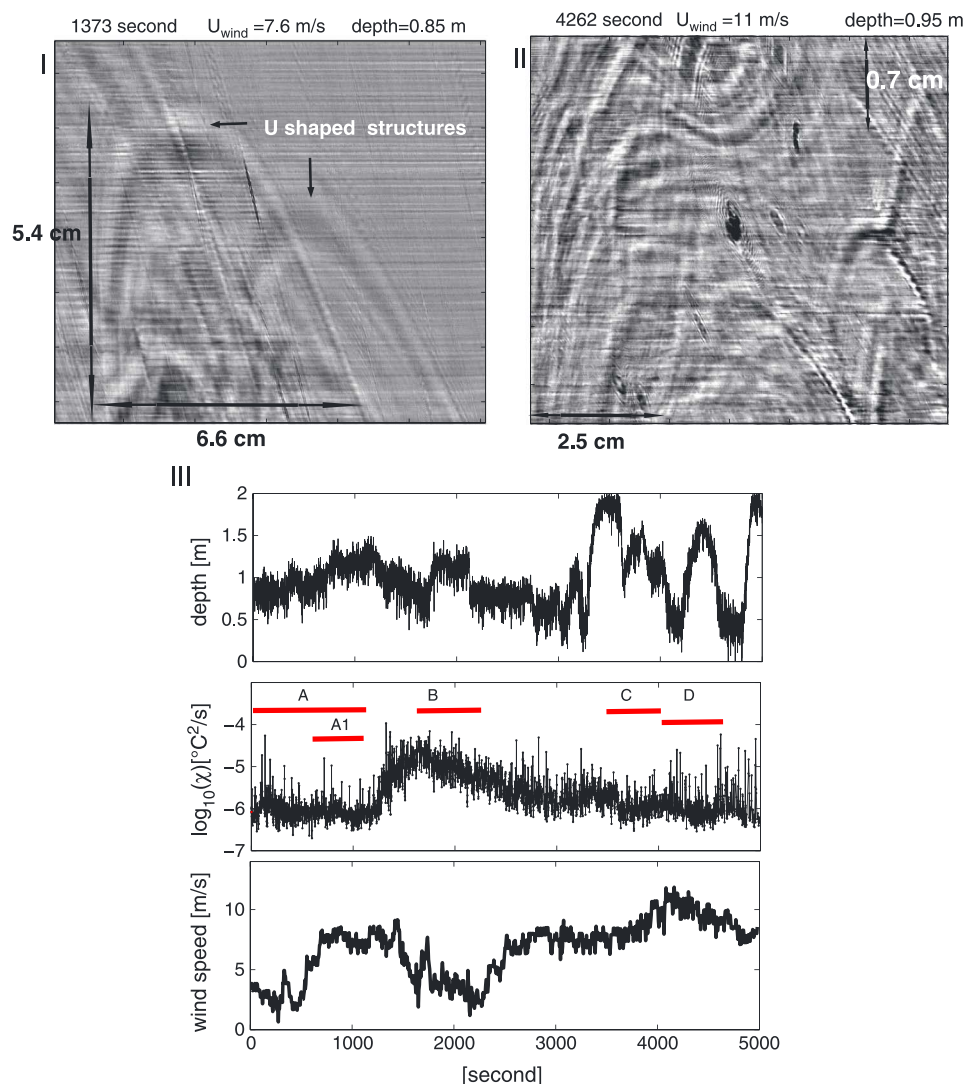


Figure 1. U-shaped coherent structures visible in the OTS image at (a) $t = 1373$ s, collected 100 s after the conclusion of the segment A/A1 and (b) for the segment D. Note the smaller structures for the segment D when the wind speed was higher (11 m/s versus 7.6 m/s). Images represent an inclined cut across the boundary with undetermined up/down direction. (c) The time series of OTS depth (top), TD rate (middle), and 10 m wind speed (bottom). Durations of segments A, A1, B, C, and D are marked by red lines in Figure 1c (middle).

possible to calculate local χ values from the observed temperature variance. Within the wall layer, ϵ follows equation (1), permitting us to estimate a new scaling for $\chi(z)$ as

$$\chi(z) = \frac{T_0'^2}{t_k} = T_0'^2 \left(\frac{u_{*w}^3}{\nu K} \right)^{1/2} z^{-1/2} \quad (3)$$

Next, we evaluate the proposed χ scaling in equation (3) with in situ data obtained during the 2012 Grand Lagrangian Deployment (GLAD) experiment.

5. In Situ Results From the GLAD Experiment

The GLAD experiment took place in the vicinity of the 2010 Deepwater Horizon oil spill but some 2 years later [Poje *et al.*, 2014]. The data presented in this work originated from the measurements on board the R/V *Walton Smith*, which was equipped with standard meteorological sensors, augmented with an air-sea flux package. Values of χ were collected using an Optical Turbulence Sensor (OTS) that acquired 10^4

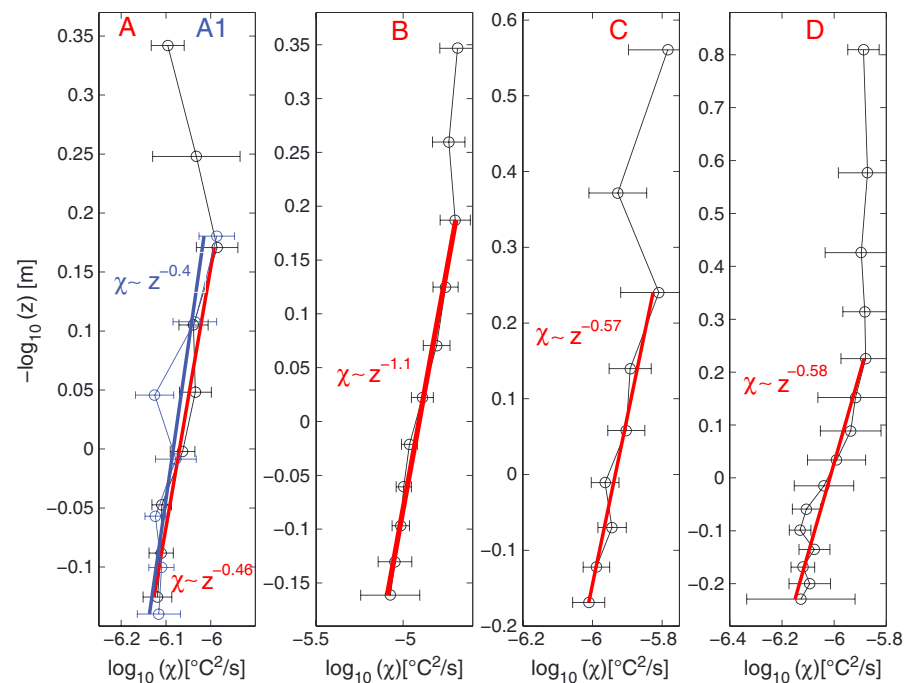


Figure 2. Vertical TD profiles in segments A, A1, B, C, and D. The error bar corresponds to the 95% confidence interval estimated using the bootstrap method [DiCiccio and Efron, 1996]. The upper part of the profile A surface to 0.67 m depth was formed and acquired (Figure 1c) during the low wind speed ≈ 3 m/s, while the deeper part from 0.67 m to 1.5 m (denoted as the profile A1 and marked by the blue line segment) was formed and acquired during the strong wind speed of 7.5 m/s. Segments A1, C, and D were characterized by wind speed in excess of 7.5 m/s. The estimated wave boundary layer corresponds to the part of the profile without line fit. The red/blue line denotes line fit to data below the wave-affected boundary.

temperature gradient spectra per second. The spectra were averaged over 1 s. For the details of the OTS operation and comparison with fast thermistor measurements, see Bogucki *et al.* [2007b]. The undulating OTS frame was towed at varying inclination to the horizontal plane effectively averaging χ values over a depth of 0.17 m. An Aquadopp current meter was mounted on the OTS frame for velocity and pressure measurements.

The data presented here were collected during a tow on 26 July 2012 starting at 20:04 UTC and lasting some 5000 s. The χ data span the depth range of $0.1 \text{ m} \leq z \leq 2 \text{ m}$ (Figure 2). To avoid the ship's wake contamination, we towed the OTS package suspended from a boom which was extended 7 m away from the ship. The towing speed was kept constant near 1 m/s. During the tow, the ship's course was held into the incoming wind and the waves to maintain the OTS upwind of the wake. In addition, it was visually verified that the ship's wake was not interfering with measurements. From the conductivity-temperature-depth vertical profile taken before the tow, it is established that the mixed layer depth was $D = 11 \text{ m}$, and the corresponding thickness of the inner boundary was around $0.2D = 2.2 \text{ m}$.

The important time scale to consider is the upper ocean $H = 1 \text{ m}$ deep response time to wind speed change. Based on the OTS temperature spectra peak location, we have estimated $\epsilon \approx 3 \cdot 10^{-6} \text{ m}^2/\text{s}^3$ within upper 2 m confirmed by microstructure shear profiler measurement during similar conditions 2 days later. Following Tennekes and Lumley [1972], the root-mean-square of the velocity fluctuation q are related to ϵ as $\epsilon = \text{const} \cdot q^3/H$ yielding $q = 0.015 \text{ m/s}$, where $\text{const} \approx 1$. The eddy viscosity K_m can be expressed [Mellor and Yamada, 1982] as $K_m = H \cdot q \cdot S = 0.0057 \text{ m}^2/\text{s}$ where $S = 0.39$. The related vertical momentum diffusion time T_{diff} , and the time scale for the upper ocean response, can be estimated as $T_{\text{diff}} = H^2/K_m = 174 \text{ s}$. All analyzed data here were at least 500 s long, thus representing equilibrated boundary response.

For the χ profile analysis, care was taken to ensure that the sampling period chosen was short enough to maintain stationarity within χ while being long enough to provide sufficient samples for the assembly of a

Table 1. Summary of Parameters During the Experiment^a

Case (Hour:Minute UTC)	A (20:04) (A1(20:15))	B (20:30)	C (20:55)	D (21:00)
Wind speed _{10m} (m/s)	5.2 (7.5)	4.1	9.1	10.1
Significant wave height H_s (m)	0.46	0.46	0.44	0.44
Dominant wave frequency (Hz)	0.11	0.11	0.11	0.11
Dominant wave speed (m/s)	14.2	14.2	14.2	14.2
Wave age (c/u_*)	86 (53)	114	45	39
Solar irradiance (W/m ²)	880	870	860	750
T_{air} (°C)	27.8	25.8	25.3	24.9
T_{water} (°C)	29.5	29.3	29.3	29.3
Monin-Obukhov depth L (m)	3 (15)	1	96	>100
z_t (m)	<0.2	<0.2	<0.2	0.2
TD wave boundary depth (m)	0.67	0.65	0.57	0.59
($\chi(z) \propto z^{-\alpha}$); exponent $\alpha \pm 95\%$ CI	0.46 ± 0.14 (0.4 ± 0.21)	1.1 ± 0.3	0.45 ± 0.23	0.58 ± 0.35

^aThe mixed layer depth D was 11 (m). The time in brackets denotes the segment start time. CI = the 95% confidence interval.

vertical χ profile. Our χ data were deemed stationary if at a given depth the collected χ values remained within the statistical scatter. To satisfy these requirements, the 5000 s long tow record was split into 500 to 1000 s long segments: A, B, C, and D (Figure 1c), where data for each segment were accumulated over the horizontal distance of around 500 to 1000 m. The Monin-Obukhov length scale was calculated from $L = (c_p \rho u_*^3) / (\alpha g Q_0 \kappa)$, where α is the thermal expansion coefficient for seawater, c_p and ρ are specific heat and density of water, g is gravitational acceleration, and Q_0 is the net heat flux at the ocean surface [Soloviev and Lukas, 2006]. Q_0 was estimated following the approach of Fairall *et al.* [1996], from collected meteorological parameters with mean observed relative humidity of around 30%. The wind stress-dominated layer, nominally extending to the depth $0.1L$, varied between 0.1 m in segment B and over 10 m for the segment D.

The summary of the background parameters during the tow is listed in Table 1. The wave height data were obtained from NOAA's Luke offshore test platform located approximately 40 km north of the tow location. The wave age c/u_* [Thorpe *et al.*, 2003] during the tow ranged from 36 to 82. The depth z_t , where ϵ attains wall layer values, is estimated in Table 1. Due to the old age of the observed waves, the relatively shallow depth $z_t = 0.2$ m was used to define the wall layer origination point.

The image of the light sheet combined with the OTS motion through the water allowed us to obtain a two-dimensional light intensity distribution—a shadowgraph image (Figures 1a and 1b). Shadowgraph images collected during GLAD frequently showed a number of coherent forms, ranging from $O(1$ cm) to much larger than image size. Among them we noted particularly the presence of U-shaped structures, which resemble packets of hairpin-like vortices observed in the wall-bounded flows [Adrian, 2007].

Results for $\chi(z)$ are presented in Figure 2 for all segments over the depth range of $0.16 \text{ m} \leq z \leq 1.6 \text{ m}$. Due to the rapid wind increase (from 5.2 m/s to 7.5 m/s; see Table 1) at the onset of the tow over segment A ($1 \leq t \leq 1200$ s of the tow; Figure 1), we have created an additional segment A1 (and the subset of A) corresponding to higher wind speeds and spanning data from the interval $700 \leq t \leq 1200$ s. The measurements contained in the profile A (Figure 2) represented a collated boundary response to changing wind speeds from 3 m/s to 7.5 m/s. That is, the part of the profile A between surface and the wave boundary layer depth 0.67 m was formed and acquired (Figure 1c) during the low wind speed 3 m/s, while the deeper part of the profile A (denoted as A1) from the 0.67 m to ≈ 1.5 m was formed and acquired during the strong wind speed of 7.5 m/s. The A1 profile was characterized by the Monin-Obukhov depth of $L = 15$ m, deeper than the mixed layer depth $D = 11$ m.

In each analyzed segment, the depth below which χ values decrease rapidly is determined. This depth is called here “the wave boundary depth,” and the corresponding values are listed in Table 1. We observe that the wave boundary depth is between $1.3H_s$ and $1.5H_s$. This is consistent with ϵ observations of Rapp and Melville [1990], noting that each profile represents an ensemble of data collected over at least 50 wave

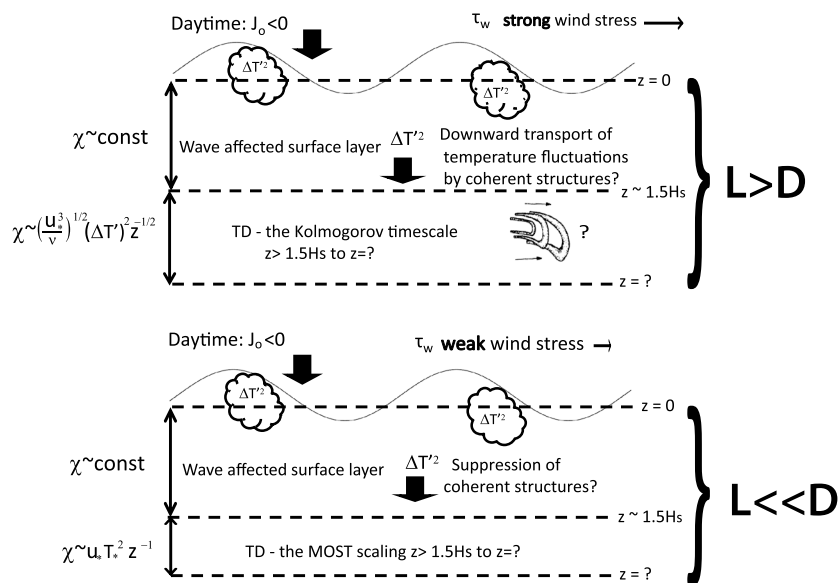


Figure 3. Schematic summary of results based on our observations. Hairpin-like structures were observed below $1.5H_s$. Question marks denote new issues arising from current study. (D is the mixed layer depth, H_s is the significant wave height, and L is the Monin-Obukhov depth.)

periods. With the wind speed over 7.1 m/s, the wind stress-dominated layer (nominal thickness $\sim 0.1L$) spanned the whole vertical observation domain; see Table 1 for segments A, A1, C, and D and Figure 2. The fit to data below the wave boundary depth reveals $\chi(z) \propto z^{-a}$ with $0.40 \leq a \leq 0.58$ for data segments A, A1, C, and D. This functional $\chi(z)$ dependence is in agreement with our postulated scaling given in equation (3).

When the wind slackened during segment B, the Monin-Obukhov depth L decreased to around 1 m and the stress-dominated region shrank to 0.1 m, indicating the dominance of buoyancy forces at depths $z > 0.1$ m. For data segment B, we find $\chi(z) \propto z^{-1.1}$ below the wave boundary layer (Figure 2). Such a scaling is consistent with the observation by Lombardo and Gregg [1989]. Note that their measurements were carried out in a convectively dominated ML, with $D < -L$ for the depth range $0.2D \leq z \leq 0.7D$. We posit that segment B is a regime when the role of near-surface coherent structures in transporting scalar variance is suppressed by the stabilizing effect of daytime buoyancy forcing (as also in the data of Lombardo and Gregg [1989] with $D < |-L|$). This makes the ocean's response to surface forcing horizontally uniform, and traditional MOST scaling of $\chi(z)$ is recovered.

6. Conclusions

We investigated the temperature dissipation rate $\chi(z)$ in the upper 2 m of the ocean under two regimes dominated by wind forcing or daytime heat flux. A summary of our findings is presented schematically in Figure 3.

We find that $\chi(z)$ remains constant for depths of 1.3 to 1.5 times the significant wave height. Below this wave boundary layer depth, χ decays as $\chi(z) \propto z^{-a}$, where the exponent a depends on the local stability conditions. When the daytime buoyancy flux dominates ($L \ll D$), we measure that $\chi(z)$ follows $\chi(z) \propto z^{-1.1}$, which is consistent with the MOST scaling of $\chi(z) \propto z^{-1}$ that applies when the ocean is subject to horizontally uniform surface forcing. However, for shear (wind forcing)-dominated cases ($L > D$), we find $\chi(z) \propto z^{-a}$ with $0.40 \leq a \leq 0.58$, which is not readily explained by the MOST scaling. We proposed a new χ scaling based on the Kolmogorov length scale, resulting in the exponent $a = 1/2$, which is consistent in our observations. At the core of this new scaling is the concept that coherent structures transport heat vertically and introduce horizontal nonuniformities in the surface forcing.

These results highlight the ocean's response to rapid changes in the surface forcing and represent a step forward in our understanding processes responsible for the ocean's heat intake.

Acknowledgments

This research was made possible by a grant from BP/The Gulf of Mexico Research Initiative. We would like to thank the crew of R/V *Walton Smith* for their assistance and Mark Graham for his help with deployment of the OTS package. Data are freely available upon request.

The Editor thanks Ren-Chieh Lien and an anonymous reviewer for their assistance in evaluating this paper.

References

- Adrian, R. J. (2007), Hairpin vortex organization in wall turbulence, *Phys. Fluids*, *19*(4), 041301.
- Anis, A. (2006), Similarity relationships in the unstable aquatic surface layer, *Geophys. Res. Lett.*, *33*, L19609, doi:10.1029/2006GL027268.
- Asher, W. E., A. T. Jessup, and M. A. Atmane (2004), Oceanic application of the active controlled flux technique for measuring air-sea transfer velocities of heat and gases, *J. Geophys. Res.*, *109*, C08S12, doi:10.1029/2003JC001862.
- Bogucki, D., and G. Spiers (2013), What percentage of the oceanic mixed layer is accessible to marine lidar? Global and the Gulf of Mexico prospective, *Opt. Express*, *21*(20), 23,997–24,014.
- Bogucki, D., J. Piskozub, M.-E. Carr, and G. Spiers (2007a), Monte Carlo simulation of propagation of a short light beam through turbulent oceanic flow, *Opt. Express*, *15*(21), 13,988–13,996.
- Bogucki, D., J. Domaradzki, C. Anderson, H. Wijesekera, R. Zaneveld, and C. Moore (2007b), Optical measurement of rates of dissipation of temperature variance due to oceanic turbulence, *Opt. Express*, *15*(12), 7224–7230.
- Bogucki, D., M.-E. Carr, W. M. Drennan, P. Woiceshyn, T. Hara, and M. Schmeltz (2010), Preliminary and novel estimates of CO₂ gas transfer using a satellite scatterometer during the 2001 GasEx experiment, *Int. J. Remote Sens.*, *31*(1), 75–92.
- Chelton, D. B., M. G. Schlax, R. M. Samelson, and R. A. de Szoeke (2007), Global observations of large oceanic eddies, *Geophys. Res. Lett.*, *34*, L15606, doi:10.1029/2007GL030812.
- Chung, D., and G. Matheou (2012), Direct numerical simulation of stationary homogeneous stratified sheared turbulence, *J. Fluid Mech.*, *696*, 434–467.
- Craig, P. D., and M. L. Banner (1994), Modeling wave-enhanced turbulence in the ocean surface layer, *J. Phys. Oceanogr.*, *24*(12), 2546–2559.
- Crone, T., and M. Tolstoy (2010), Magnitude of the 2010 Gulf of Mexico oil leak, *Science*, *330*, 634.
- Cross, J., W. A. M. Nimmo-Smith, P. J. Hosegood, and R. Torres (2014), The dispersal of phytoplankton populations by enhanced turbulent mixing in a shallow coastal sea, *J. Mar. Syst.*, *136*, 55–64.
- Dalgleish, F., W. Hou, A. Vuorenkoski, G. Nootz, and B. Ouyang (2013), In situ laser sensing of mixed layer turbulence, in *Ocean Sensing and Monitoring V*, vol. 8724, edited by W. W. Hou and R. A. Arnone, Proc. SPIE, Baltimore, Md., 29 April, doi:10.1117/12.2019193.
- DiCiccio, T. J., and B. Efron (1996), Bootstrap confidence intervals, *Stat. Sci.*, *11*, 189–212.
- Fairall, C. W., E. F. Bradley, D. P. Rogers, J. B. Edson, and G. S. Young (1996), Bulk parameterization of air-sea fluxes for Tropical Ocean-Global Atmosphere Coupled-Ocean Atmosphere Response Experiment, *J. Geophys. Res.*, *101*(C2), 3747–3764.
- Hartogensis, O., and H. A. R. Debruin (2005), Monin-Obukhov similarity functions of the structure parameter of temperature and turbulent kinetic energy dissipation rate in the stable boundary layer, *Boundary Layer Meteorol.*, *116*(2), 253–276.
- Hinze, J. O. (1959), *Turbulence: An Introduction to Its Mechanism and Theory*, 586 pp., McGraw-Hill, New York.
- Hunt, J. C., and J. F. Morrison (2000), Eddy structure in turbulent boundary layers, *Eur. J. Mech. B. Fluids*, *19*(5), 673–694.
- Jernelöv, A., and O. Lindén (1981), IXTOC I: A case study of the world's largest oil spill, *Ambio*, *10*(6), 299–306.
- Khakpour, H. R., T. Igusa, and L. Shen (2012), Coherent vortical structures responsible for strong flux of scalar at free surface, *Int. J. Heat Mass Transfer*, *55*(19), 5157–5170.
- Klein, P., and G. Lapeyre (2009), The oceanic vertical pump induced by mesoscale and submesoscale turbulence, *Annu. Rev. Mar. Sci.*, *1*(1), 351–375, doi:10.1146/annurev.marine.010908.163704.
- Komori, S., R. Kurose, K. Iwano, T. Ukai, and N. Suzuki (2010), Direct numerical simulation of wind-driven turbulence and scalar transfer at sheared gas-liquid interfaces, *J. Turbul.*, *11*, 1–20.
- Large, W. G., J. C. McWilliams, and S. C. Doney (1994), Oceanic vertical mixing: A review and a model with a nonlocal boundary layer parameterization, *Rev. Geophys.*, *32*(4), 363–403.
- Lévy, M., D. Iovino, L. Resplandy, P. Klein, G. Madec, A.-M. Tréguier, S. Masson, and K. Takahashi (2011), Large-scale impacts of submesoscale dynamics on phytoplankton: Local and remote effects, *Ocean Model.*, *44*, 77–93, doi:10.1016/j.ocemod.2011.12.003.
- Li, M., and C. Garrett (1998), The relationship between oil droplet size and upper ocean turbulence, *Mar. Pollut. Bull.*, *36*(12), 961–970.
- Lombardo, C. P., and M. C. Gregg (1989), Similarity scaling of viscous and thermal dissipation in a convecting surface boundary layer, *J. Geophys. Res.*, *94*, 6273–6284.
- Lozano-Durán, A., and J. Jiménez (2014), Time-resolved evolution of coherent structures in turbulent channels: Characterization of eddies and cascades, *J. Fluid Mech.*, *759*, 432–471.
- Mellor, G. L., and T. Yamada (1982), Development of a turbulence closure model for geophysical fluid problems, *Rev. Geophys.*, *20*(4), 851–875.
- Nowell, A. R. (1983), The benthic boundary layer and sediment transport, *Rev. Geophys.*, *21*(5), 1181–1192.
- Osborn, T. R., and C. S. Cox (1972), Oceanic fine structure, *Geophys. Astrophys. Fluid Dyn.*, *3*(1), 321–345.
- Poje, A. C., et al. (2014), Submesoscale dispersion in the vicinity of the Deepwater Horizon spill, *Proc. Natl. Acad. Sci.*, *111*, 12,693–12,698.
- Rapp, R., and W. Melville (1990), Laboratory measurements of deep-water breaking waves, *Philos. Trans. R. Soc. London, Ser. A*, *331*, 735–800.
- Sander, J., A. Simon, T. Jonas, and A. Wüest (2000), Surface turbulence in natural waters: A comparison of large eddy simulations with microstructure observations, *J. Geophys. Res.*, *105*(C1), 1195–1207.
- Shay, T. J., and M. Gregg (1986), Convectively driven turbulent mixing in the upper ocean, *J. Phys. Oceanogr.*, *16*(11), 1777–1798.
- Soloviev, A., and R. Lukas (2006), *The Near-Surface Layer of the Ocean: Structure, Dynamics and Applications*, vol. 31, 572 p., Springer, Berlin.
- Soloviev, A. V., and P. Schlüssel (1996), Evolution of cool skin and direct air-sea gas transfer coefficient during daytime, *Boundary Layer Meteorol.*, *77*(1), 45–68.
- Tennekes, H., and J. L. Lumley (1972), *A First Course in Turbulence*, 301 pp., MIT Press, Cambridge, Mass.
- Terray, E., M. Donelan, Y. Agrawal, W. Drennan, K. Kahma, A. Williams, P. Hwang, and S. Kitaigorodskii (1996), Estimates of kinetic energy dissipation under breaking waves, *J. Phys. Oceanogr.*, *26*(5), 792–807.
- Thorpe, S., T. Osborn, J. Jackson, A. Hall, and R. Lueck (2003), Measurements of turbulence in the upper-ocean mixing layer using Autosub, *J. Phys. Oceanogr.*, *33*(1), 122–145.
- Trenberth, K. (2002), Earth system processes, in *Encyclopedia of Global Environmental Change*, edited by M. C. McCracken and J. S. Perry, pp. 13–30, John Wiley, Chichester, U. K.